J. Fluid Mech. (2000), *vol.* 405, *pp.* 57–77. Printed in the United Kingdom

Rayleigh–Marangoni oscillatory instability in a horizontal liquid layer heated from above: coupling and mode mixing of internal and surface dilational waves

By A. Ye. REDNIKOV[1,2], P. COLINET[1,2], M. G. VELARDE[1] AND J. C. LEGROS[2]

[1] Instituto Pluridisciplinar, Universidad Complutense de Madrid, Paseo Juan XXIII, 1, Madrid 28040, Spain
[2] Université Libre de Bruxelles-MRC, Chimie-Physique EP, CP 165/62, Av. F. D. Roosevelt, 50, Bruxelles 1050, Belgium

(Received 29 July 1997 and in revised form 6 October 1999)

An oscillatory instability mechanism is identified for a horizontal liquid layer with undeformable open surface heated from the air side. Although buoyancy and surface tension gradients are expected to play a stabilizing role in this situation, we show that, acting together, they may lead to the instability of the motionless state of the system. The instability is a consequence of the coupling between internal and surface waves, whose resonant interaction and resulting mode mixing are discussed. Predictions amenable to experimental test are given together with a thorough analytical and numerical study of the problem.

1. Introduction

Two wave motions are possible at the open surface of a liquid or at the interface between two liquids. These are the capillary–gravity waves (Lamb 1945) and the dilational waves (Lucassen 1968*a*, *b*). One mechanism capable of exciting such waves is the Marangoni effect, i.e. surface stresses and subsequent flow motions due to surface tension gradients along the surface or interface (Levich 1962; Lucassen 1968*a*, *b*). The Marangoni effect may be due to heat or (surfactant) mass transfer across (i.e. transversally to) or along (longitudinally to) the surface or interface. When such transport is induced by suitably imposed transverse gradients the possibility exists of sustaining these waves past an instability threshold (Sternling & Scriven 1959; Reichenbach & Linde 1981; Takashima 1981; Levchenko & Chernyakov 1981; Garcia-Ybarra & Velarde 1987; Chu & Velarde 1988, 1989).

Sternling & Scriven (1959) considered the case of two semi-infinite liquid layers separated by an undeformable interface, and showed that overstability and wave motions are possible, in particular when the heat transfer occurs out of the phase with higher kinematic viscosity and thermal diffusivity. A liquid–air system satisfies this criterion when the heating is imposed from the air side, which was indeed confirmed by Reichenbach & Linde (1981), who generalized the analysis to finite-depth layers. In both these works, the importance of convective heat transport in the gas phase was pointed out. Moreover, with little or no surface deformation, the unstable modes correspond to dilational waves, i.e. motions mostly along the interface. Hence, these modes are also called longitudinal waves.

Still for a liquid layer heated from above, but ignoring the influence of the overlying gas, Takashima (1981) considered the active role of surface deformation and also located an overstability threshold. His numerical results were supported by the subsequent analytical study of Garcia-Ybarra & Velarde (1987) who showed that the energy input due to the Marangoni effect is indeed able to sustain *transverse* capillary–gravity waves. They also pointed out the relevance of their findings for variable and eventually microgravity conditions. Takashima (1981) did not discuss dilational waves. At about the same time, Levchenko & Chernyakov (1981) considered both types of waves induced and sustained by the Marangoni effect when heating a Bénard layer from the air side, and discussed the possible resonance between these two wave modes. Later on, Chu & Velarde (1988, 1989) and Hennenberg *et al.* (1992) also considered both kinds of waves, in connection with various thermal and solutal Marangoni effects. Earnshaw & McLaughlin (1991, 1993) also considered the resonance between both kinds of waves, though in a situation where they are not sustained by the Marangoni effect. An extension of Levchenko & Chernyakov's analysis to the situation where the upper phase is a liquid has recently been provided by Rednikov *et al.* (1998).

On the other hand, if a liquid layer open to air is heated from below, it is known that steady cellular convection is possible past an instability threshold due to either unstable stratification induced by buoyancy (Rayleigh 1916), or surface tension gradients, hence the Marangoni effect (Koschmieder 1993). Pearson (1958) was the first to unambiguously clarify theoretically the role of surface tension gradients in Bénard experiments. He considered a liquid layer open to air heated from the bottom side and neglected surface deformation. No oscillatory instability was found and could not be expected for Pearson's model problem, for either way of heating, as shown by Vidal & Acrivos (1966). Nield (1964) considered the combined effect of buoyancy and the Marangoni effect, heating a liquid layer from below, and still no surface deformation. Oscillatory instability was not considered by Nield. Koschmieder (1993) has provided a comprehensive account of these two mechanisms of steady, cellular instability (see also Normand, Pomeau & Velarde 1977; Busse 1978; Velarde & Normand 1980). Finally, it is known that if in a (not too shallow) Bénard layer the heating is from the air side with gravity pointing vertically downwards, the fluid layer may exhibit *internal* waves, i.e. damped oscillatory motions with the Brunt–Väisälä frequency, as in the atmosphere or the ocean.

Thus, it appears clearly that when dealing with a Bénard layer open to air with a deformable liquid–air interface, heating from below or above in the presence of gravity, a rich variety of phenomena and instabilities is expected. Old and recent experiments by Linde and coworkers have illustrated this wealth of phenomena (Weidman, Linde & Velarde 1992; Velarde *et al.* 1995; Linde *et al.* 1997; Wierschem *et al.* 1999). No author has yet discussed the problem in its full generality. There are too many parameters and possible complex instability mechanisms. We shall not do it here. Rather, in view of the known results, we shall stick as much as possible to a realizable experiment, and rely on this to simplify the problem. In such an experiment, the usual set-up would be a closed system where temperature is controlled below at the solid support of the liquid and at a higher value at a solid plate above the air gap overlying the liquid. For not too shallow liquid layers, surface deformation is negligible, and if the air gap above the liquid is thin enough, it can be modelled by a suitable Biot number. Then, an interesting and realistic problem is reduced to Nield's formulation with, however, the possibility of the appearance of internal waves due to a stable density stratification. Justification of these simplifications will be given later on.

What can be expected in Nield's formulation that has been overlooked by earlier authors? We shall show here that when heating a liquid layer from above, although buoyancy merely allows damped internal waves and the Marangoni effect may not be able to sustain dilational surface waves, yet the coupling of these two effects is capable of triggering an instability allowing both (internal and dilational) waves to be sustained past an instability threshold.

The text is organized as follows. In § 2 the linear stability problem is formulated. In § 3 we provide numerical predictions about marginal stability conditions. Further understanding of these results is obtained in § 4 through an asymptotic analysis for high enough (in absolute value) negative Rayleigh and Marangoni numbers, which allows to unambiguously distinguish between *internal* waves and dilational, or as mentioned above, longitudinal *surface* waves and to study their resonance. Further discussion of the results is given in § 5. A discussion of the possible role of both surface deformation and the dynamics of the air gap is also provided there. Then, a weakly nonlinear analysis is presented in § 6 to clarify the nature of the transition at the bifurcation point. Finally, in § 7, we provide some conclusions.

2. Formulation of the linear stability problem

Consider a liquid layer of infinite horizontal extent ($-\infty < x < \infty$) and depth h, subjected to a constant vertical temperature gradient β ($\beta > 0$ when heating from below and $\beta < 0$ otherwise). The layer rests on a flat rigid bottom ($z = 0$). Its upper free surface is assumed to be undeformable and open to air (Bénard layer). Dimensionless quantities are defined using the following scales: h for length, h^2/χ for time, χ/h for velocity, $\mu\chi/h^2$ for pressure and βh for temperature, where μ is the dynamic viscosity and χ is the thermal diffusivity. Assuming the Boussinesq approximation to be valid (Chandrasekhar 1961; Perez-Cordon & Velarde 1975; Velarde & Perez-Cordon 1976; de Boer 1984, 1986), the linearized equations and boundary conditions for the amplitudes of the normal modes with growth rate Λ and wavenumber k, $\exp(\Lambda t + \mathrm{i}kx)$, are (see Nield 1964)

$$\mathrm{i}kU + W_z = 0, \tag{1}$$

$$Pr^{-1}\Lambda U = -\mathrm{i}kP + \left(U_{zz} - k^2 U\right), \tag{2}$$

$$Pr^{-1}\Lambda W = -P_z + RT + \left(W_{zz} - k^2 W\right), \tag{3}$$

$$\Lambda T - W = T_{zz} - k^2 T, \tag{4}$$

$$z = 0: \qquad U = W = T = 0, \tag{5}$$

$$z = 1: \qquad W = U_z + Mik T = T_z + Bi\, T = 0, \tag{6}$$

with

$$Pr \equiv \frac{\nu}{\chi}, \quad R \equiv \frac{\alpha\beta g h^4}{\nu\chi}, \quad Bi \equiv \frac{\kappa_s h}{\kappa}, \quad M \equiv -\frac{\mathrm{d}\sigma}{\mathrm{d}T}\frac{\beta h^2}{\mu\chi}$$

where U, W, P and T are (amplitudes of) horizontal and vertical components of the velocity field, pressure and temperature disturbances, respectively. The subscript z refers to the corresponding derivative, g is the value of gravity acceleration, ν is the kinematic viscosity, α is the thermal expansion coefficient, κ is the thermal conductivity, κ_s is a constant heat transfer coefficient at the open surface, σ is the surface tension and $\mathrm{d}\sigma/\mathrm{d}T$ is its variation with temperature (generally negative). Pr,

R, Bi and M are Prandtl, Rayleigh, Biot and Marangoni numbers, respectively. The second part in the interfacial boundary conditions (6) results from the tangential stress balance (Marangoni effect), while the third one expresses the energy balance.

This is exactly the problem posed by Nield (1964), and corresponds well to standard experiments for Bénard steady cellular convection (Koschmieder 1993). However, in contrast with Nield, we here seek overstability ($\mathrm{Im}\Lambda \neq 0$) at $R < 0$ and $M < 0$, which in the standard case ($\alpha > 0$, $\mathrm{d}\sigma/\mathrm{d}T < 0$) corresponds to heating the Bénard layer from the air side or cooling it from below ($\beta < 0$).

3. Marginal conditions ($\mathrm{Re}\Lambda = 0$) for oscillatory instability ($\mathrm{Im}\Lambda \neq 0$). Numerical results

First, we solve equations (1)–(4) with all boundary conditions (5), (6) but without using the Marangoni stress condition in (6). Then, using the latter yields the solvability condition in the form of a dispersion relation, which can be formally rewritten as $M = f(\Lambda, k, Pr, Bi, R)$. With M real, we have in fact two relations $M = \mathrm{Re}\, f(\Lambda, k, Pr, Bi, R)$ and $\mathrm{Im}\, f(\Lambda, k, Pr, Bi, R) = 0$, allowing us to determine the growth rate $\mathrm{Re}\,\Lambda$ and the frequency $\omega = \mathrm{Im}\,\Lambda$. As we look for the marginal states we set $\Lambda = \mathrm{i}\omega$ and solve $\mathrm{Im}\, f = 0$ for the critical frequency ω of expected oscillations, at constant k, Pr, Bi, and R (this is done by numerically tracing the zeros of $\mathrm{Im}\, f = 0$). Then, $M = \mathrm{Re}\, f$ yields the corresponding critical value of the Marangoni number.

Two representations of the marginal curve (Marangoni number versus wavenumber) will be used hereafter, according to whether we fix the Rayleigh number, or the *dynamic* Bond number $B \equiv R/M$. Note that in the latter case, the complex solvability condition $M = f(\mathrm{i}\omega, k, Pr, Bi, B, M)$ is solved iteratively (Newton–Raphson method) for M and ω. The first representation (fixed R) allows qualitative comparison with the case of surface-tension-gradient-driven (Marangoni) instability in a layer with deformable interface, when the Galileo number $G = gh^3/\nu\chi$ is held fixed (see § 5.2). The second representation is a more physical one, since B does not depend on the temperature gradient, and is therefore fixed by the choice of a given set-up and liquid.

Examples of marginal curves at fixed Rayleigh number are shown in figure 1(a), while the frequency along those states is plotted in figure 1(b). The solid lines labelled 1 and 2 correspond to $R = -3 \times 10^6$ and $R = -1.5 \times 10^6$, respectively. The point marked 3 corresponds to $R = -1.21 \times 10^6$. In all cases we have chosen, for illustration, $Pr = 6$ and $Bi = 0$. For completeness, the broken lines correspond to results obtained in § 5. The marginal curves appear in the form of a 'bubble' whose interior corresponds to the region of instability. The bubble and its actual form depend crucially on the fixed Rayleigh number. Indeed, as the absolute value of R is lowered, the bubble becomes smaller and smaller and finally collapses to the point 3 at $R = -1.21 \times 10^6$. This corresponds to the minimum value of $-R$ allowing oscillatory instability. As the absolute value of R is increased, the bubble grows and is shifted to higher absolute values of M.

The general scenario (see also § 5) is that in principle, at $R \to -\infty$, a countable number of bubbles should appear, corresponding to a countable number of vertical modes ($n = 1, 2, \ldots$). The bubble shown in figure 1 corresponds to the fundamental mode ($n = 1$). Each mode has its own minimum value of $-R$, increasing with n. For example, the second bubble ($n = 2$) emerges (from a point) only at $R = -5.29 \times 10^7$. The third bubble ($n = 3$) appears at $R = -4.68 \times 10^8$, and so on.

The 'bubble' form of marginal curves in this first representation (M versus k, at fixed R) deserves clarification. It does not imply that in an experiment, increasing the

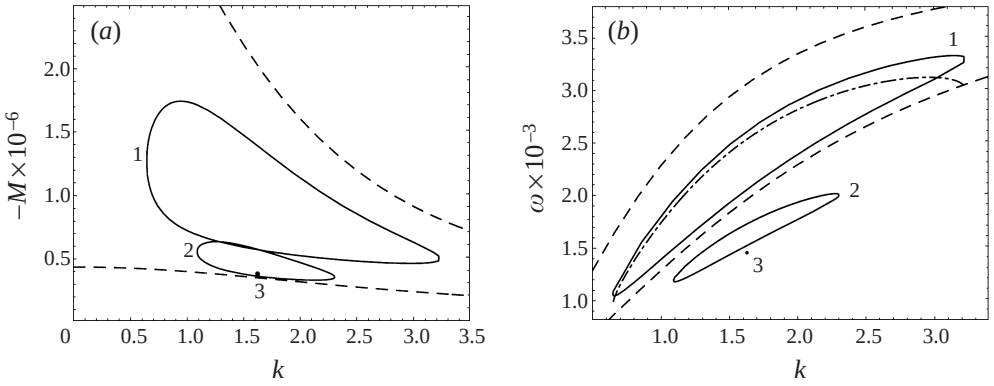

FIGURE 1. (*a*) Marginal stability curves, and (*b*) critical frequency, for the lowest unstable mode *at fixed Rayleigh number*, $Pr = 6$ and $Bi = 0$: solid line 1 for $R = -3 \times 10^6$, solid line 2 for $R = -1.5 \times 10^6$. The point 3 corresponds to $R = -1.21 \times 10^6$, below which (in absolute value) no marginal states exist. Broken lines show the asymptotic results (equations (28), (29), (22), (23), $n = 1$, $R = -3 \times 10^6$, $Pr = 6$, $Bi = 0$, $M = RB$). The upper and lower curves correspond to *surface* and *internal* waves, respectively. The dot-dashed line is obtained by formally plotting the surface wave frequency (equation (23)) along the numerically found marginal states. Note that varying the thermal gradient changes both Rayleigh and Marangoni numbers, and hence the figure must be taken as a cross-section of a three-dimensional (M, k, R) surface.

temperature gradient one could de-stabilize and then re-stabilize the rest state. As an increase of $-M$ is always accompanied by an increase of $-R$ (both are proportional to the temperature difference), the upper part of the growing bubble is actually never crossed (alternatively, figure 1 can be viewed in a three-dimensional perspective). This is better seen using the more practical representation at fixed $B = R/M$, and not at fixed R. Figure 2 shows the marginal curves (*a*) and the corresponding frequencies (*b*) at fixed B and again $Pr = 6$ and $Bi = 0$ for $B = 1.5;\ 2;\ 4;\ 6;\ 10;$ and 15. The broken line is the locus of the minima as B is varied. With increasing B, the minimum shifts from long waves ($k \to 0$) to short waves ($k \to \infty$). The lowest absolute value of the critical Marangoni number is achieved for intermediate values of B, which represent the optimal balance between the Marangoni and Rayleigh effects. $B = 0.715$ is the lowest possible value, below which the marginal curves disappear at infinity with $k \to 0$. For the second mode ($n = 2$) the lowest possible Bond number is $B = 6.44$ (see also analytical results in § 5). Thus for $B > 6.44$ the corresponding marginal curves also exist. However, they lie well beyond the range of figure 2 and thus are not displayed. Similar behaviour occurs for the higher-order modes ($n = 3, 4, \ldots$).

Nield's type of marginal stability diagram (in the plane $\{-M, -R\}$) is represented in figure 3(*a*). For a given B, the intersection of the straight line $R = BM$ with the marginal curve of figure 3(*a*) yields the critical temperature gradient for the onset of instability. No more than one point of intersection is expected. The lower branch of the marginal curve has an oblique asymptote with slope 0.715 (at large absolute values of R and M), in accordance with the fact that for $B < 0.715$ the marginal states do not exist. The critical wavenumber tends to zero along the lower branch, and diverges to infinity along the upper branch. Note that the extrema of the bubble in the fixed-R representation and the minima of the neutral curves in the fixed-B representation are in fact one and the same point, belonging to the marginal curve of figure 3(*a*). For illustration, figure 3(*b*) also contains the results for two higher-order modes ($n = 2$ and $n = 3$).

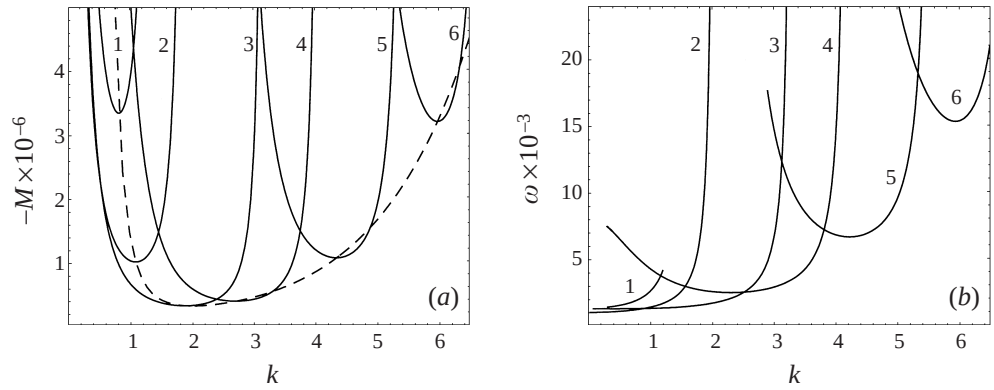

FIGURE 2. (*a*) Marginal stability curves, and (*b*) critical frequency, for the fundamental mode *at fixed dynamic Bond number* ($B \equiv R/M$), $Pr = 6$ and $Bi = 0$: curve 1 $B = 1.5$, curve 2 $B = 2$, curve 3 $B = 4$, curve 4 $B = 6$, curve 5 $B = 10$, curve 6 $B = 15$. When B is varied, the minimum of the marginal curve moves along the dashed line.

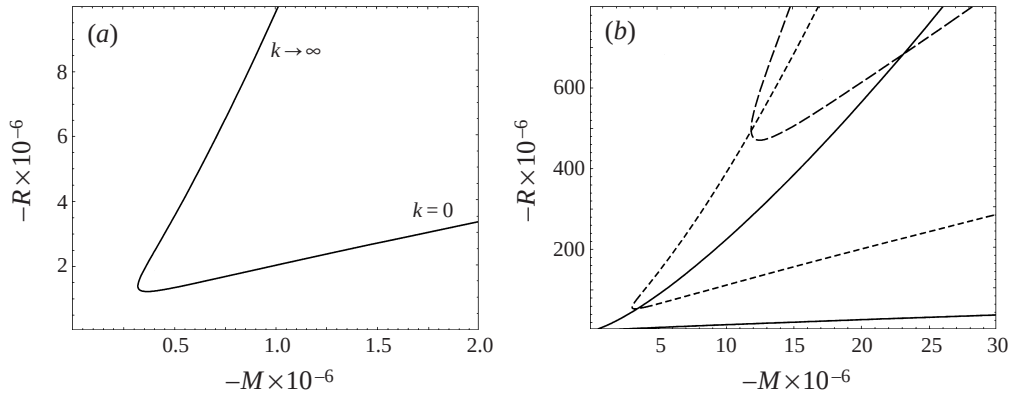

FIGURE 3. Stability boundary in the plane $\{-M, -R\}$ at $Pr = 6$ and $Bi = 0$. (*a*) The fundamental mode ($n = 1$), (*b*) modes $n = 1$ (solid line), $n = 2$ (short-dashed line) and $n = 3$ (long-dashed line).

Figure 4(*a–d*) illustrates the influence of the Prandtl and Biot numbers on Nield's diagram (*a*), and on the variations with dynamic Bond number of critical Marangoni number (*b*), wavenumber (*c*) and frequency (*d*). In particular, we observe that lowering Pr (enhancing inertia) and Bi (reducing heat dissipation to the upper gas layer) yields lower instability thresholds.

4. The limit of large negative Rayleigh and Marangoni numbers. Internal and surface waves

To get a deeper understanding of the structure of the perturbation fields within the liquid layer, associated with the wave modes described above, we now provide an asymptotic analysis taking advantage of the expected high (absolute) values of the Rayleigh and Marangoni numbers.

4.1. *Dispersion relation*

For high enough absolute values of Rayleigh and Marangoni numbers, the time scales $|\alpha\beta g|^{-1/2}$ and $|\rho h^2/((\mathrm{d}\sigma/\mathrm{d}T)\beta)|^{1/2}$, associated with possible *internal* and *surface*

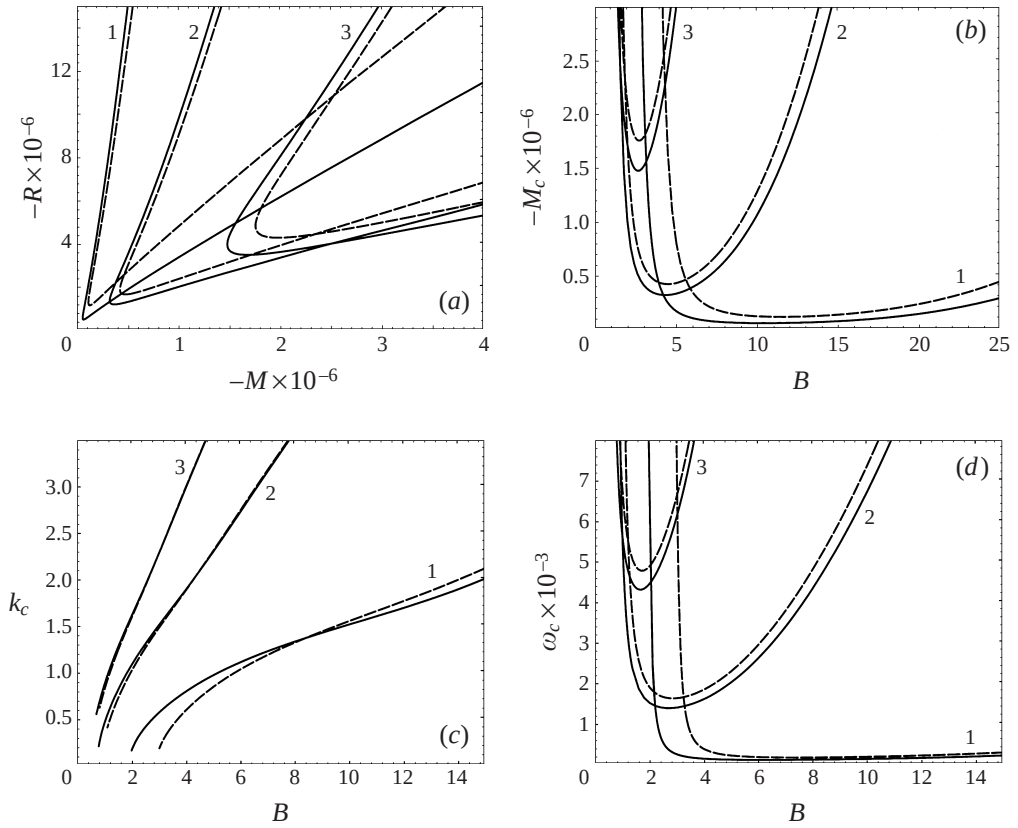

FIGURE 4. (*a*) Stability boundary in the plane $\{-M,-R\}$, (*b*) critical Marangoni number, (*c*) wavenumber and (*d*) frequency, *versus* dynamic Bond number at various values of the Prandtl and Biot numbers. The three pairs of curves correspond to $Pr = 0.1$, $Pr = 6$ and $Pr = 20$, marked 1, 2 and 3, respectively. Within each pair, the solid and broken lines are for $Bi = 0$ and $Bi = 1$, respectively.

motions are much faster than the characteristic viscous and thermal time scales, h^2/ν and h^2/χ (ρ is the mean density). These fast time scales yield corresponding scales for velocity and pressure, which e.g. for buoyancy-induced internal motions are $|\alpha\beta g h^2|^{1/2}$ and $|\rho\alpha\beta g h^2|$, respectively. For convenience, in order to start the asymptotic expansions with terms of order unity, we rewrite the system (1)–(6) using these scales. Then we have

$$\mathrm{i}ku + w_z = 0, \tag{7}$$

$$\lambda u = -\mathrm{i}kp + \epsilon^2\left(u_{zz} - k^2 u\right), \tag{8}$$

$$\lambda w = -p_z - T + \epsilon^2\left(w_{zz} - k^2 w\right), \tag{9}$$

$$\lambda T - w = \frac{\epsilon^2}{Pr}\left(T_{zz} - k^2 T\right), \tag{10}$$

$$z = 0: \qquad u = w = T = 0, \tag{11}$$

$$z = 1: \qquad w = u_z - \frac{1}{B\epsilon^2}\mathrm{i}kT = T_z + Bi\,T = 0 \tag{12}$$

with

$$\epsilon \equiv \left(-\frac{Pr}{R}\right)^{1/4} \ll 1, \qquad B \equiv \frac{R}{M},$$

where here lower-case symbols λ, u, w and p denote the same quantities as the upper-case ones in (1)–(6). The second part of (12) is the Marangoni stress condition.

Then, in the leading-order approximation in ϵ, the action of the dissipative terms in equations (8)–(10) is limited to boundary layers at the bottom and at the open surface, while in the bulk the flow is inviscid. The smallness parameter ϵ is just of order of the boundary layer thickness. We look for the solution separately in each one of these three regions, subsequently using the appropriate matching procedure. Accordingly, we introduce the stretched vertical variables

$$\bar{z} = \frac{1-z}{\epsilon}, \quad \tilde{z} = \frac{z}{\epsilon}$$

and develop all components of the function $f = (u, w, p, T)$ in power series

$$f(z) = f_0 + \epsilon f_1 + \cdots \tag{13}$$

in the bulk;

$$f(\bar{z}) = \bar{f}_0 + \epsilon \bar{f}_1 + \cdots \tag{14}$$

in the surface boundary layer; and

$$f(\tilde{z}) = \tilde{f}_0 + \epsilon \tilde{f}_1 + \cdots \tag{15}$$

in the bottom boundary layer.

The only exception is the horizontal velocity in the free-surface boundary layer, which is sought in the form

$$u(\bar{z}) = \epsilon^{-1}\bar{u}_{(-1)} + \bar{u}_0 + \cdots, \tag{16}$$

i.e. we start with the term of order ϵ^{-1}. The justification of this choice will be provided later on.

After substituting (13)–(16) into (7)–(12) we get a hierarchy of linear problems corresponding to $\epsilon^n (n = -1, 0, 1, \ldots)$. At each step a solvability condition must be satisfied providing a dispersion relation.

In the bottom boundary layer, (7) yields that $\tilde{w}_0$ is constant, while due to the second boundary condition (11) this constant is zero. Then the matching condition between $\tilde{w}_0$ and w_0 yields $w_0 = 0$ at $z = 0$. Using this, the solution of (7)–(10) in the bulk is

$$p_0 = c \cosh\left(\sqrt{\frac{\lambda^2+1}{\lambda^2}}kz\right), \quad u_0 = -\frac{\mathrm{i}k}{\lambda} c \cosh\left(\sqrt{\frac{\lambda^2+1}{\lambda^2}}kz\right),$$

$$w_0 = -c\frac{k}{\lambda}\sqrt{\frac{\lambda^2}{\lambda^2+1}} \sinh\left(\sqrt{\frac{\lambda^2+1}{\lambda^2}}kz\right). \tag{17}$$

In the open surface boundary layer we have

$$\bar{u}_{(-1)} = c_1 \exp\left(-\sqrt{\lambda}\bar{z}\right) \tag{18}$$

where $\sqrt{\lambda}$ is taken with positive real part.

Then according to (7)

$$\bar{w}_0 = \frac{\mathrm{i}kc_1}{\sqrt{\lambda}}\left[1 - \exp\left(-\sqrt{\lambda}\bar{z}\right)\right].$$

The matching between $\bar{w}_0$ and w_0 yields

$$c_1 = \frac{\mathrm{i}c}{\sqrt{\lambda}}\sqrt{\frac{\lambda^2}{\lambda^2+1}}\sinh\left(\sqrt{\frac{\lambda^2+1}{\lambda^2}}k\right).$$

For the temperature field in the open surface boundary layer, using (10) and the third boundary condition (12), we have

$$\bar{T}_0 = \frac{\mathrm{i}kc_1}{\lambda\sqrt{\lambda}} + \frac{\mathrm{i}kc_1}{\lambda\sqrt{\lambda}}\frac{Pr}{1-Pr}\exp\left(-\sqrt{\lambda}\bar{z}\right) - \frac{\mathrm{i}kc_1}{\lambda\sqrt{\lambda}}\frac{Pr^{1/2}}{1-Pr}\exp\left(-\sqrt{\lambda}Pr^{1/2}\bar{z}\right).$$

As Bi is assumed to be of order unity, while the boundary layer is thin, the results do not depend on the Biot number at this stage.

Finally, using the thermocapillary (Marangoni stress) boundary condition (12), which is in fact the solvability condition in our scheme, we get the dispersion relation

$$\sinh\left(\sqrt{\frac{\lambda^2+1}{\lambda^2}}k\right)\left(\lambda^2 + \frac{k^2}{B(Pr^{1/2}+1)}\right) = 0. \tag{19}$$

The solutions of (19) are

$$\lambda_0^2 = -\frac{k^2}{k^2+\pi^2n^2} \quad (n = 1, 2, \ldots), \qquad \lambda_0^2 = -\frac{k^2}{B(Pr^{1/2}+1)}. \tag{20}$$

The subscript 0 is used to recall that this is actually the leading-order result. Thus in the leading-order approximation, λ is purely imaginary. We will discuss these solutions in the next subsection. Here note only that without starting the expansion (16) for the horizontal velocity in the upper boundary layer at the order ϵ^{-1}, we would have lost the second solution (20).

To obtain the real part of λ, it is necessary to consider the next-order correction. Let us first consider the bottom boundary layer. Equation (8) becomes $\lambda\tilde{u}_0 = -\mathrm{i}k\tilde{p}_0 + \tilde{u}_{0\tilde{z}\tilde{z}}$. According to (9), $\tilde{p}_0$ and $\bar{p}_0$ are constants, which are equal to the value of p_0 at $z = 0$ and $z = 1$, respectively. Using the first boundary condition (11) as well as matching to the zeroth-order solution in the bulk, we get

$$\tilde{u}_0 = -\frac{\mathrm{i}k}{\lambda}c\left[1 - \exp\left(-\sqrt{\lambda}\tilde{z}\right)\right].$$

Then

$$\tilde{w}_1 = -\frac{k^2}{\lambda}c\tilde{z} + \frac{k^2}{\lambda\sqrt{\lambda}}c\left[1 - \exp\left(-\sqrt{\lambda}\tilde{z}\right)\right].$$

The matching condition between $\tilde{w}_0 + \epsilon\tilde{w}_1$ and $w_0 + \epsilon w_1$ provides the boundary condition for w_1 at $z = 0$. Then, the solution in the bulk, still inviscid in this approximation, is

$$w_1 = c\frac{k^2}{\lambda\sqrt{\lambda}}\cosh\left(\sqrt{\frac{\lambda^2+1}{\lambda^2}}kz\right).$$

Then, in the upper boundary layer we get

$$\bar{u}_0 = c_2\exp\left(-\sqrt{\lambda}\bar{z}\right) - \tfrac{\mathrm{i}k}{\lambda}c\cosh\left(\sqrt{\tfrac{\lambda^2+1}{\lambda^2}}k\right),$$

$$\bar{w}_1 = \tfrac{k^2}{\lambda}c\cosh\left(\sqrt{\tfrac{\lambda^2+1}{\lambda^2}}k\right)\bar{z} + \tfrac{\mathrm{i}kc_2}{\sqrt{\lambda}}\left[1 - \exp\left(-\sqrt{\lambda}\bar{z}\right)\right].$$

The matching condition between $\bar{w}_0 + \epsilon\bar{w}_1$ and $w_0 + \epsilon w_1$ yields

$$c_2 = -\frac{\mathrm{i}k}{\lambda} c \cosh\left(\sqrt{\frac{\lambda^2+1}{\lambda^2}}k\right).$$

Finally, calculating $\bar{T}_1$ in the upper boundary layer, using the thermocapillary boundary condition (12), and taking into account, simultaneously, the two orders of approximation, we get

$$\begin{aligned}
&\sqrt{\frac{\lambda^2}{\lambda^2+1}}\sinh\left(\sqrt{\frac{\lambda^2+1}{\lambda^2}}k\right)\left(\lambda^2 + \frac{k^2}{B(Pr^{1/2}+1)}\right)\\
&-\epsilon\frac{k}{\sqrt{\lambda}}\cosh\left(\sqrt{\frac{\lambda^2+1}{\lambda^2}}k\right)\left(\lambda^2 + \frac{k^2}{B}\frac{2Pr^{1/2}+1}{Pr^{1/2}(Pr^{1/2}+1)}\right)\\
&-\epsilon\frac{k^2}{\sqrt{\lambda}}\frac{Bi}{BPr^{1/2}(1+Pr^{1/2})}\sqrt{\frac{\lambda^2}{\lambda^2+1}}\sinh\left(\sqrt{\frac{\lambda^2+1}{\lambda^2}}k\right) = 0. \qquad (21)
\end{aligned}$$

This is an approximate dispersion relation, which we now analyse in detail.

4.2. *Marginal stability*

In the leading order, (21) yields the purely imaginary solutions (20). Rewriting them, using now the thermal time scale as $\Lambda^2 = -\omega^2$, we get

$$\omega^2 = -RPr\frac{k^2}{k^2+\pi^2n^2} \quad (n = 1, 2, \ldots) \qquad (22)$$

and

$$\omega^2 = -M\frac{Pr}{Pr^{1/2}+1}k^2. \qquad (23)$$

Equation (22) yields the (Brunt–Väisälä) frequency of the *internal* waves in a stably stratified inviscid liquid layer (Normand *et al.* 1977), while (23) accounts for the frequency of dilational (or longitudinal) *surface* waves. Note that the former depends only on R, while the latter is only function of M. The latter wave is *genuinely dissipative* (Lucassen 1968*a*, *b*; Sternling & Scriven 1959; Levchenko & Chernyakov 1981; Chu & Velarde 1988, 1989). Recall that no surface deformation exists in our Rayleigh–Marangoni problem. Fluid motion in the surface wave is accompanied by an intense *horizontal* velocity field in the surface boundary layer ($c_1 \neq 0$ in (18)), while for the internal wave $c_1 = 0$, and the velocity field is of the same order of magnitude everywhere.

The *resonance* between *internal* and dilational *surface* waves occurs when the frequencies (22) and (23) are equal to each other. Thus at resonance

$$B_{res}(k, n, Pr) = \frac{k^2+\pi^2n^2}{Pr^{1/2}+1} \quad (n = 1, 2, \ldots). \qquad (24)$$

Proceeding to the next-order correction in (21), we represent the eigenvalue λ as

$$\lambda = \lambda_0 + \epsilon\lambda_1 + \cdots \qquad (25)$$

where λ_0 is defined by (20), corresponding to the internal and surface waves, respec-

tively. Using (25) in (21) we find

$$\left[\lambda_0^2 + \frac{k^2}{B(Pr^{1/2}+1)}\right]\lambda_1 + (\lambda_0^2+1)\sqrt{\lambda_0}\left[\lambda_0^2 + \frac{k^2}{B}\frac{2Pr^{1/2}+1}{Pr^{1/2}(Pr^{1/2}+1)}\right] = 0 \qquad (26)$$

for the internal wave, and

$$2\sqrt{\frac{\lambda_0^2}{\lambda_0^2+1}}\sinh\left(\sqrt{\frac{\lambda_0^2+1}{\lambda_0^2}}k\right)\lambda_1 + k\sqrt{\lambda_0}\frac{Pr^{1/2}+1}{Pr^{1/2}}\cosh\left(\sqrt{\frac{\lambda_0^2+1}{\lambda_0^2}}k\right)$$
$$+BiPr^{-1/2}\sqrt{\lambda_0}\sqrt{\frac{\lambda_0^2}{\lambda_0^2+1}}\sinh\left(\sqrt{\frac{\lambda_0^2+1}{\lambda_0^2}}k\right) = 0 \qquad (27)$$

for the surface wave.

The sign of $\mathrm{Re}\lambda_1$ determines whether the corresponding wave is damped or amplified. Imposing $\mathrm{Re}\lambda_1 = 0$ in (26), (27), we get the conditions of marginal stability:

$$B_{int}(k,n,Pr) = \frac{2Pr^{1/2}+1}{Pr^{1/2}(Pr^{1/2}+1)}\left[k^2+\pi^2n^2\right] \quad (n=1,2,\ldots) \qquad (28)$$

for the internal wave, and

$$B_{sf}(k,n,Pr) = \frac{1}{Pr^{1/2}+1}\left[k^2+s^2(n)\right] \quad (n=1,2,\ldots) \qquad (29)$$

for the surface wave, respectively. Here $s(n)$ are the solutions of the equation

$$\cos(s) + \frac{Bi}{1+Pr^{1/2}}\frac{\sin(s)}{s} = 0$$

and, in particular, at $Bi = 0$, we get $s(n) = \pi(n-1/2)$.

Note that we always have $B_{sf} < B_{res} < B_{int}$. The instability associated with the internal mode ($\mathrm{Re}\lambda_1 > 0$ in (26)) takes place for $B_{res} < B < B_{int}$. The surface mode yields instability ($\mathrm{Re}\lambda_1 > 0$ in (27)) for $B_{sf} < B < B_{res}$. Thus, the regions of instability in the '*B versus k*' plane are confined by the inequalities $B_{sf} < B < B_{int}$ $(n = 1, 2\ldots)$.

4.3. *Mode mixing at resonance*

The divergence of λ_1 when it is calculated with the help of equations (26) and (27) in the vicinity of the resonance, demands a more refined analysis. It is clear that when the coefficient of λ_1 becomes too small, one must also take into account the quadratic term ($\sim \lambda_1^2$) when deriving an equation for λ_1 from (21). The most general case of this asymptotics corresponds to $(B - B_{res})/B_{res} \equiv \epsilon^{1/2}\delta \sim \epsilon^{1/2}$ and $\lambda_1 \equiv \epsilon^{-1/2}\bar{\lambda}_1 \sim \epsilon^{-1/2}$. Then we have

$$\frac{2}{\bar{\lambda}_0}\bar{\lambda}_1^2 + \delta\bar{\lambda}_1 - (\bar{\lambda}_0^2+1)\sqrt{\bar{\lambda}_0}\frac{Pr^{1/2}+1}{Pr^{1/2}} = 0 \qquad (30)$$

where $\bar{\lambda}_0$ is chosen to coincide with λ_0 for the internal wave (first equation (20)). Note that the correction to the eigenvalue, although higher at resonance ($\epsilon^{1/2}$, while earlier it was of order ϵ), still remains small.

Near resonance, the zeroth-order eigenvalues for the two modes (equation (20)) coincide, and a possible difference appears only in the first-order approximation. Accordingly, (30) has two solutions for $\bar{\lambda}_1$. Note that, first, there are no marginally stable states in the vicinity of the resonance point. Second, one of the solutions $\bar{\lambda}_1$ of (30) has always positive real part, while the other is negative. Consequently, the

resonance occurs only when one of the two modes is unstable, while the other is stable.

In the region $|\delta| \gg 1$, $\bar{\lambda}_0 + \epsilon^{1/2}\bar{\lambda}_1$ should match with $\lambda_0 + \epsilon\lambda_1$ for the internal and surface waves, taken at $B \to B_{res}$, with λ_0 given by (20) and λ_1 obtained from (26), (27). The asymptotics of one of the solutions of (30) at $|\delta| \gg 1$ is

$$\bar{\lambda}_1 \approx (\bar{\lambda}_0^2 + 1)\sqrt{\bar{\lambda}_0}\frac{Pr^{1/2} + 1}{Pr^{1/2}}/\delta + \cdots$$

for $\delta > 0$, and

$$\bar{\lambda}_1 \approx -\tfrac{1}{2}\bar{\lambda}_0\delta - (\bar{\lambda}_0^2 + 1)\sqrt{\bar{\lambda}_0}\frac{Pr^{1/2} + 1}{Pr^{1/2}}/\delta + \cdots$$

for $\delta < 0$.

Using the matching procedure described above, it follows that the mode corresponding to this solution turns into the internal wave at $\delta > 0$, $|\delta| \gg 1$ while it becomes the surface wave at $\delta < 0$, $|\delta| \gg 1$. At the same time, waves are amplified. One can also show that just the opposite holds for the second solution of (30). Thus, near resonance there is a continuous transition from the *internal* wave mode to the *surface* one, and vice versa, and hence we have *mode mixing*. A salient characteristic of this transition is a higher degree of damping/amplification. At resonance both modes resemble more an internal wave mode, since their corresponding leading-order frequencies coincide and, as a consequence, $c_1 = 0$ in (18). Accordingly, neither of the two modes has an intense horizontal velocity component in the surface boundary layer.

5. Discussion of results

5.1. *Comparison of analytical and numerical results*

Broken lines in figure 1(*a*) show the results (28) and (29), where the representation of marginal curves at fixed Rayleigh number is used, for $n = 1$ and $R = -3 \times 10^6$ – the same as for bubble 1 ($M = RB$). We observe that they approach the lower and the upper sides of the bubble. However, this value of $(-R)$ is not large enough, in absolute value, to achieve a good quantitative agreement with the exact numerical results. As R is increased in absolute value and the bubble grows, the agreement is improved. Thus, at $R \to -\infty$, the lower and upper branches of the bubble tend to the marginal curves for the internal and surface waves, respectively. The actual form of the bubble depends crucially on the value given to the Rayleigh number. The region of instability corresponds to the interior of the bubble. Qualitatively, at given Rayleigh number, the instability is associated with the internal waves in the lower part of the bubble (below the resonance curve), and with dilational surface waves in the upper part of the bubble. This is exactly what happens in the limit $R \to -\infty$.

The fact that the boundary layer approach does not work for too long or too short waves and cannot account for the left and right rounded parts that join upper and lower parts of each bubble can be seen as follows. As $k \to 0$, the frequencies (22) and (23) both decay as $\omega \sim k$. At $k \sim \epsilon^2 \sim |R|^{-1/2}$, the time scale for the internal and surface oscillations is no longer faster than the viscous and thermal time scales. For $k \to \infty$, the viscous and thermal time scales decay faster (as k^{-2}) than that for surface and, moreover, internal waves, becoming of the same order as the latter at $k \sim \epsilon^{-1} \sim |R|^{1/4}$. Thus the region of validity is $O(|R|^{-1/2}) \ll k \ll O(|R|^{1/4})$.

The results (28), (29) should be understood in the sense of the limit $R \to -\infty$. They yield a *countable* number of bubbles ($n = 1, 2 \ldots$) whose left and right rounded zones have gone to $k = 0$ and $k = \infty$, respectively. For whatever large but finite $(-R)$,

only a finite number of bubbles exists. The higher is n, the higher should be R (in absolute value) to achieve a satisfactory agreement with the numerical results for the corresponding bubble.

The lower and upper broken lines in figure 1(b) correspond to the leading-order frequencies of internal (equation (22)) and surface waves (equation (23)), respectively (for $n = 1$ and $R = -3 \times 10^6$ – again the same as for bubble 1). The latter is drawn along the marginal states (29). Alternatively, if we draw the surface wave frequency along the *numerically* determined marginal states (the upper branch of bubble 1 in figure 1a), we get the dot-dashed line (figure 1b), obtaining a better agreement with the corresponding numerical result. We observe that at moderately large ($-R$) and ($-M$) the asymptotic expressions for the frequencies (22) and (23) work better than that for the marginal curves (28) and (29).

Returning to the representation at a fixed B, we introduce $k_{res}(B, n, Pr)$, $k_{int}(B, n, Pr)$ and $k_{sf}(B, n, Pr)$ as the roots of the equations $B_{res}(k, n, Pr) = B$, $B_{int}(k, n, Pr) = B$ and $B_{sf}(k, n, Pr) = B$, respectively. Note that always $k_{int} < k_{res} < k_{sf}$. If there is no corresponding root, we will formally regard k_{res}, k_{int} or k_{sf} as zero. The interval of instability corresponds to $k_{int} < k < k_{sf}$. On the diagram of figure 2, $k = k_{int}$ and $k = k_{sf}$ define the left and right vertical asymptotes of the marginal curve, respectively. For the examples of figure 2 we find: (1) $k_{int} = 0$, $k_{sf} = 1.65$; (2) $k_{int} = 0$, $k_{sf} = 2.11$; (3) $k_{int} = 0$, $k_{sf} = 3.37$; (4) $k_{int} = 0$, $k_{sf} = 4.27$; (5) $k_{int} = 2.11$, $k_{sf} = 5.66$; (6) $k_{int} = 3.41$, $k_{sf} = 7.02$. Note that $k_{sf} \neq 0$ appears starting from $B > 0.715$. This is in agreement with the fact that $B = 0.715$ is the lowest possible value for oscillatory instability of the mode $n = 1$ (for $Pr = 6, Bi = 0$), as discussed in § 3. Equation (29) also permits us to calculate the lowest possible values of B for the higher-order modes. For example, for $n = 2$ we have $B = 6.44$, and $B = 17.9$ for $n = 3$, and so on.

If k_{res} is not zero, it splits the instability interval into two parts. The left and the right parts correspond to instability of internal and surface waves, respectively. Accordingly, in this case, the branch of the marginal curve approaching the left asymptote corresponds to internal waves, while the branch at the right asymptote corresponds to surface waves. Shown in figure 5 is the frequency drawn along the marginal states. The solid line corresponds to the exact, numerical solution for the example 4 of figure 2(b). The long-dashed curve is obtained by plotting the leading-order surface wave frequency (23) along the numerically determined marginal curve 4 of figure 2(a), while the short-dashed curve is the corresponding one for the internal wave frequency (22). The former becomes indistinguishable from the solid line on the right, while the same occurs for the latter on the left, as expected.

The asymptotic theory developed in the previous section gives the asymptotes (i.e. the interval of unstable wavenumbers in the limit of high absolute values of Rayleigh and Marangoni numbers, $R \to -\infty$, $M \to -\infty$). If we add the next-order terms ($O(\epsilon) = O(|R|^{-1/4}) = O(|M|^{-1/4})$) into (26), (27), we can in principle calculate how the marginal curves tend to the asymptotes. However, calculation of the marginal curve on the whole interval $k_{int} < k < k_{sf}$ (and thus the calculation of the critical conditions) lies beyond the possibilities of our asymptotic analysis, since otherwise we would need to balance (empirically) terms of different orders in ϵ. This in fact shows that asymptotically the minima correspond to $R \sim 1$ and $M \sim 1$, although they appear to be numerically large in practice. At this level, we cannot speak about internal and surface waves in the strict asymptotic sense, as done above. However, as (22), (23) for the frequencies work well beyond the region where the overall asymptotic picture (corresponding to the limit $R \to -\infty$, $M \to -\infty$) holds qualitatively, the possibility exists of using these concepts in a wider (qualitative) sense.

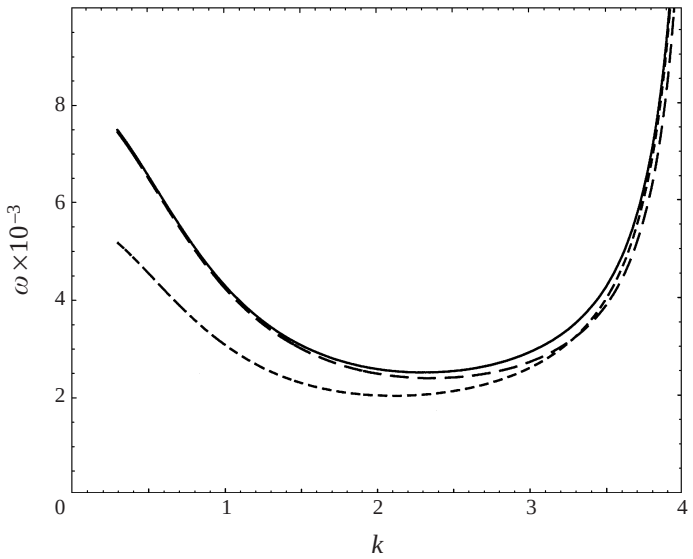

FIGURE 5. Comparison of exact and asymptotic dispersion relations for Rayleigh–Marangoni waves. The solid line reproduces curve 4 of figure 2(*b*). The long- and short-broken lines are obtained by plotting the frequencies of the *internal* (equation (22), $n = 1$) and *surface* (equation (23)) waves, respectively, along the corresponding marginal curve of figure 2(*a*).

To illustrate the relevance of our findings to experiments, let us estimate the critical temperature difference, βh, for the onset of oscillatory instability. Take typical parameters of water: $\rho \approx 1\,\mathrm{g\,cm^{-3}}$, $\nu \approx 10^{-2}\,\mathrm{cm^2\,s^{-1}}$, $\chi \approx 0.14\times10^{-2}\,\mathrm{cm^2\,s^{-1}}$, $\mathrm{d}\sigma/\mathrm{d}T \approx -0.17\,\mathrm{dyn\,cm^{-1}\,K^{-1}}$ and $\alpha \approx 0.5\times10^{-3}\,\mathrm{K^{-1}}$ (at 50 °C). Then $B \approx 2.5h^2$. Take e.g. $B \approx 5$, which approximately corresponds to the lowest value of the critical Marangoni number (figure 2*a*). Then $h \approx 1.4\,\mathrm{cm}$. As $M_c \approx 3 \times 10^5$ (figure 2*a*), the critical temperature difference, δT, is

$$\delta T \sim 15\,\mathrm{K} \tag{31}$$

which can be easily achieved in experiment (Linde *et al.* 1997; Wierschem *et al.* 1999).

5.2. *Dilational versus capillary–gravity waves: the role of a deformable surface*

When surface deformation is taken into account in a Bénard layer, overstability has been predicted (Takashima 1981). Physically, this instability is associated with the interaction between capillary–gravity and dilational surface waves (Levchenko & Chernyakov 1981; Chu & Velarde 1988, 1989; Rednikov *et al.* 1998). Thus, it is worth considering here the analogy between the coupling, resonance and mode mixing in the two problems: capillary–gravity versus dilational waves, and internal versus dilational waves. In both cases, a pair of high-frequency wave modes exists, one of which is just the dilational or longitudinal surface wave with first-order dispersion relation (23). The other wave is the internal one in the case treated here, (22), and the capillary–gravity wave in the case of a layer with deformable interface. The latter problem requires the definition of the Galileo number

$$G = \frac{gh^3}{\nu\chi} = \frac{B_s}{Cr} \tag{32}$$

where the *static* Bond number is

$$B_s = \frac{\rho g h^2}{\sigma}$$

and the capillary (crispation) number

$$Cr = \frac{\rho \nu \chi}{\sigma h}.$$

Here, we have considered a limiting case where the internal-wave time scale $|\alpha\beta g|^{-1/2}$ is much smaller than the viscous and thermal dissipation scales, and hence a high enough Rayleigh number (in absolute value). At large Galileo number (which is typical of most experiments with Bénard layers), the time scale of gravity waves at the open deformable surface, $(h/g)^{1/2}$, is also much smaller than the dissipative time scales. In the same units as used for equations (22) and (23), and considering $B_s = O(1)$, the frequency of capillary–gravity waves is then given by

$$\omega^2 = Pr\, G\, k \left(1 + \frac{k^2}{B_s}\right) \tanh(k). \tag{33}$$

Comparing the dispersion relations (22), (23) and (33), it appears that the frequency of dilational waves may not only become identical to that of internal waves (when (24) holds, i.e. $M \sim R$) for some $k = O(1)$, but also to that of capillary–gravity waves (when $M \sim G$). Although the physical mechanisms underlying these waves are different, features of mode mixing at resonance turn out to be similar (Rednikov *et al.* 1998).

Nevertheless, in addition to the fact that internal–dilational and (capillary) gravity–dilational resonance points are usually well separated (because $G \gg R$, see § 5.4), some qualitative differences are also expected. Among these, let us first note that, as said earlier, here we have a *countable* number of potentially overstable modes ($n = 1, 2\ldots$), given by the Brunt–Väisälä relationship (22). Another difference is that here the marginal curves are in the form of a bubble (figure 1*a*), while for the Bénard layer with deformable surface they form an open 'bag', which is confined from the side of short waves as well, but however has no left rounded zone. Rather, its upper and lower branches approach a vertical asymptote at $k = 0$. From this point of view, it looks reasonable that a lowest possible Rayleigh number exists, corresponding to the bubble collapse. However no lower bound for the Galileo number has been found in the surface-tension-gradient-driven problem with deformable surface, since as the latter is decreased the right rounding zone of the bag simply moves to longer waves, while preserving its topological shape.

5.3. *Role of the air gap above the liquid*

The oscillatory instability described by Sternling & Scriven (1959) and Reichenbach & Linde (1981) is clearly due to the active role of the air, or more precisely, to the convective heat transport therein. Indeed, overstability is ruled out if the gas phase is assumed passive, i.e. if heat transport is only accounted for by a Biot number (Vidal & Acrivos 1966). Yet, the order of magnitude of the critical Marangoni number and the value of the frequency obtained by Reichenbach & Linde (1981) are about the same as in the present study. The question then arises of which mechanism will first lead to instability.

First, note that as the thickness of the air gap above the liquid is decreased, the critical Marangoni number rapidly increases, as can be shown for the case studied by Reichenbach & Linde (1981). Indeed, as for the instability to exist it is necessary that the conductive heat transport is not predominant with respect to the convective

one, the thinner the air layer is, the higher should be the frequency (and relative velocity amplitude) to maintain this balance, and thus, the higher should be the critical Marangoni number.

On the other hand, for the Rayleigh–Marangoni instability analysed here, diminishing the air gap thickness does not lead to such drastic consequences. Indeed, with a rather thin air gap (long-wave limit in the air layer), and moreover, with a large gas-to-liquid ratio of thermal diffusivities (usually, about 10^2), heat transport is mainly diffusive in the air gap. Then its description in terms of a Biot number becomes appropriate, and a simple computation yields

$$Bi = \delta_\kappa / \delta_h$$

where δ_κ is the gas-to-liquid ratio of heat conductivities, and δ_h is the corresponding ratio of layer depths. At the same time, poor heat conductivity of the air ($\delta_\kappa \ll 1$) permits moderate Biot numbers even for shallow air layers ($\delta_h \ll 1$), so that the critical Marangoni number and frequency remain of the same order as for $Bi = 0$. For instance, if we assume $\delta_h = \frac{1}{10}$ (i.e. 1.4 mm air gap in the numerical example (31)), while typically $\delta_\kappa = \frac{1}{20}$, we get $Bi = 0.5$, a rather moderate value indeed. In such conditions, our predicted instability is dominant relative to that found by Reichenbach & Linde (1981).

As a side remark, note that the vertical temperature gradient needed for instability does not necessarily come from a temperature difference between the rigid bottom of the liquid layer and the rigid top of the overlying gas layer (in a closed set-up), as implied above. For example, the liquid layer can be heated by means of surface heat generation, as assumed by Levchenko & Chernyakov (1981). Then, due to the poor heat conductivity of the air, almost all heat goes to the liquid layer, and thus, the role of the air gap becomes negligible. Then, the Biot number can be set to zero.

5.4. *Further remarks on the possible role of surface deformability*

Let us now discuss the role of surface deformability in view of earlier findings (Takashima 1981; Levchenko & Chernyakov 1981; Garcia-Ybarra & Velarde 1987; Chu & Velarde 1988). First, figure 1 in Takashima's (1981) paper shows that the critical Marangoni number significantly grows with increasing *static* Bond number B_s, and thus, with increasing liquid layer thickness. Moreover, the simultaneous decrease of the capillary number Cr contributes to the further increase of the critical Marangoni number. These features are well captured by the asymptotic result obtained by Levchenko & Chernyakov (1981) for the critical Marangoni number

$$M_c = \frac{Pr + Pr^{1/2}}{2Pr^{1/2} + 1} G. \tag{34}$$

Equation (34) is valid if $G \gg 1$, where G is defined by (32). In most experiments with Bénard layers, G is at least of order of 10^5. For water ($\nu = 10^{-2}\,\mathrm{cm^2\,s^{-1}}$, $\chi = 10^{-3}\,\mathrm{cm^2\,s^{-1}}$), with $h = 1$ mm, G is about 10^5. Then, if $h \sim 1$ cm, as for the standard experiment earlier suggested, we get $G \sim 10^8$, and according to (34), $M_c \sim 10^8$, thus much higher than the corresponding value in our Rayleigh–Marangoni case. Moreover, $M_c \sim 10^8$ is unrealistic for standard experiments on Marangoni convection. Thus, this indicates that surface deformability has negligible role in the Rayleigh–Marangoni problem treated here.

On the other hand, the Rayleigh–Marangoni instability mechanism described in this work does not contribute to the overstability for liquid layers that are too shallow, of order of 1 mm or less (the *dynamic* Bond number is too small). One can therefore

conclude that the action of each of the two mechanisms is limited to a different region of the parameter space of the problem, and the regions apparently do not intersect.

Another asymptotic result for oscillatory Marangoni instability in a layer with deformable open surface (Levchenko & Chernyakov 1981; Garcia-Ybarra & Velarde 1987; Chu & Velarde 1988) is (in our notation)

$$M_c = 7.93(PrG)^{3/4}/B_s^{1/8} \tag{35}$$

with

$$k_c = \sqrt{5B_c}\,. \tag{36}$$

This result is valid for relatively thick liquid layers, much thicker than the capillary length (i.e. $B_s \gg 1$), and $G \gg 1$. As seen from (36), the critical wavelength is determined by this capillary length, and corresponds to a short-wave instability ($k_c \gg 1$). Due to the different powers of the Galileo number, (35) yields a lower threshold for thick layers than (34), and an additional estimate is necessary. For $h \sim 1\,\mathrm{cm}$, $\nu \sim 10^{-2}\,\mathrm{cm^2\,s^{-1}}$, $\chi \sim 10^{-3}\,\mathrm{cm^2\,s^2}$, we have $G \sim 10^8$. For simplicity consider $B_s^{1/8} \sim 1$ (although $B_s \gg 1$, the power $\frac{1}{8}$ practically offsets it). Then (35) yields $M_c \sim 10^7$, which is still higher than the threshold in the Rayleigh–Marangoni problem ($M_c \sim 3 \times 10^5$).

If the above arguments are disregarded, and the problem is nevertheless formulated to include, simultaneously, buoyancy and surface deformability, due care must be given to consider possible consequences of this step, that may amount to the necessity of using a non-Boussinesq approach. Indeed, this inevitably brings the Galileo number into the problem, in addition to the Rayleigh number. Instead of R and G, the independent parameters can be taken to be R and $\alpha\beta h = R/G$. Then, on the one hand, the Boussinesq approximation implies that the smallness parameter $\alpha\beta h$ can be neglected everywhere, except for the buoyancy factor (i.e. the Rayleigh number here). On the other hand, if buoyancy is studied in conjunction with surface deformability, this parameter is brought back as independent. Therefore, to be consistent, it may be necessary to go beyond the Boussinesq approximation by keeping the terms of order $\alpha\beta h$, associated with the thermal dependence of density, however small they might be. Besides, if so, there is no reason to neglect effects due to the thermal variations of other fluid properties (like viscosity).

Therefore, surface deformability is actually a non-Boussinesq correction (Davis & Segel 1968). It is small, as argued above. However, the high (absolute) values of the critical Rayleigh and Marangoni numbers (and as a consequence, temperature difference) obtained here give rise to a question about other possible corrections, and how strong they are. Apparently, most important of them are those that result from the temperature dependence of viscosity (usually much stronger than that of density), and the possible nonlinear profile of stratification. Surface deformability is expected to be weaker, as it is closely related to the thermal variation of density. Estimation of the latter, for our quantitative example (31), yields $\alpha\beta h \sim 10^{-2}$, i.e. quite small.

6. Weakly nonlinear analysis

To get further understanding on the nature of the transition from the rest state to wave behaviour, we now consider the problem in a close vicinity of the oscillatory instability threshold. As seen in figure 3(*a*), for a fixed $B = R/M$ and at some critical

$M = M_c(B)$, a pair of complex-conjugate eigenvalues, $\lambda = \pm i\omega_c$, acquires a positive real part. The corresponding critical wavenumber, k_c, is finite, at least for values of B which are neither too small nor too large (see also figure 2). Thus for waves expected at $M = M_c$, we can write (at the leading order)

$$f(x,z,t) = A_+ \exp[i(k_c x + \omega_c t)]U_c(z) + A_- \exp[i(k_c x - \omega_c t)]U_c^*(z) + \text{c.c.} \tag{37}$$

where c.c. and the star denote the complex conjugate. The quantity f stands for any perturbation field, and f_c for the corresponding component of the critical eigenvector, while A_+ and A_- are amplitudes of left- and right-travelling waves respectively. For simplicity, we restrict consideration to two-dimensional waves.

Using the scalings $A_\pm = \epsilon^{1/2} a_\pm$, $M - M_c \sim \epsilon$, it is possible to follow the time-variation of the amplitudes on a slow scale, $t_1 = \epsilon t$. At order $\epsilon^{1/2}$, we get the linear problem, whose solution is just equation (37). At order ϵ, non-secular corrections proportional to $\exp[i(\pm k_c x \pm \omega_c t)] \times \exp[i(\pm k_c x \pm \omega_c t)]$ are found, while at order $\epsilon^{3/2}$, the cancellation of secular contributions yields the set of coupled Landau equations (rewritten in terms of unscaled variables):

$$\left.\begin{aligned} \dot{A}_+ &= A_+(\sigma_0\delta - \alpha|A_+|^2 - \beta|A_-|^2), \\ \dot{A}_- &= A_-(\sigma_0^*\delta - \alpha^*|A_-|^2 - \beta^*|A_+|^2), \end{aligned}\right\} \tag{38}$$

where $\delta = (M - M_c)/M_c$, the dot denotes derivative with respect to t, and σ_0, α and β are complex coefficients depending on the values of B, Pr and Bi. As the procedure for calculating them is now classical (Normand *et al.* 1977; Knobloch 1986; Renardy 1993), we do not provide more details here but rather turn directly to the analysis of results.

Apart from the basic state $A_+ = A_- = 0$ (unstable for $\sigma_{0R}\delta > 0$), other fixed points of (38) are travelling waves (TW) for which $|A_+|^2 = \sigma_{0R}\delta/\alpha_R$, $A_- = 0$ (corresponding to left-TW, while the right-TW are given by $|A_-|^2 = \sigma_{0R}\delta/\alpha_R$, $A_+ = 0$), and standing waves (SW) for which $|A_+|^2 = |A_-|^2 = \sigma_{0R}\delta/(\alpha_R + \beta_R)$. Here the subscript R denotes the real part. The imaginary parts of (38) account for corrections to the critical frequency.

The linear stability analysis of these wave solutions yields that for $0 < \alpha_R < \beta_R$, the TW are stable (respectively, SW are unstable), and for $0 < \alpha_R, -\alpha_R < \beta_R < \alpha_R$, the SW are stable (respectively, TW are unstable). In all other cases, both waves are unstable, and the system (38) blows up after finite time, indicating that higher-order terms must be included in the Landau equations (38) to have nonlinear saturation. Typical values of the coefficients σ_0, α and β are provided in Table 1, for $Pr = 0.1$ and $Pr = 6$, and in both cases for $Bi = 0$. Some values of B have been chosen in the vicinity of the part of Nield's marginal curve (see figure 3*a*) yielding the lowest instability threshold (i.e. that corresponding to the optimal balance between buoyancy and surface tension effects). Note that the normalization condition adopted for the critical eigenfunctions is $T_c(z = 1) = 1$, which is responsible for the high numerical values of coefficients α and β. It is seen that for all cases investigated, $0 < \alpha_R, -\alpha_R < \beta_R < \alpha_R$, and hence SW is the only stable solution for $\delta > 0$. It also appears that the frequency of SW increases with increasing supercriticality δ. The data of table 1 also indicate that the amplitude of surface temperature fluctuations is usually very small for moderate δ, and rather unobservable in experiments. However, taking into account the large absolute values of critical Marangoni and Rayleigh numbers, it can be calculated that the velocity fluctuations and in particular the surface velocities are easily measurable quantities.

Pr	B	$-M_c \times 10^{-6}$	K_c	ω_c	σ_0	$\alpha \times 10^{-6}$	$\beta \times 10^{-6}$
6	3	0.4116	1.506	1405	$20.4 + 689\mathrm{i}$	$4.64 - 4.36\mathrm{i}$	$0.80 + 3.83\mathrm{i}$
6	4	0.3236	1.888	1612	$23.4 + 791\mathrm{i}$	$3.50 - 2.11\mathrm{i}$	$1.08 + 2.68\mathrm{i}$
6	5	0.3330	2.287	2017	$26.0 + 991\mathrm{i}$	$3.80 + 0.28\mathrm{i}$	$1.66 + 1.17\mathrm{i}$
0.1	5.2	0.1493	0.998	114.3	$1.56 + 56.1\mathrm{i}$	$0.373 - 0.306\mathrm{i}$	$-0.0754 + 0.0714\mathrm{i}$
0.1	10	0.0554	1.501	116.4	$2.12 + 56.8\mathrm{i}$	$0.0759 - 0.0079\mathrm{i}$	$-0.0280 - 0.0481\mathrm{i}$
0.1	15	0.0693	1.986	184.2	$2.45 + 90.4\mathrm{i}$	$0.0901 + 0.325\mathrm{i}$	$-0.0574 - 0.379\mathrm{i}$

TABLE 1. Critical parameters and coefficients of Landau equations for zero free surface Biot number, and various Prandtl and dynamic Bond numbers.

7. Concluding remarks

It has been shown that a not too shallow Bénard layer may become oscillatorily unstable when it is heated from above or cooled from below, due to the joint action of buoyancy and thermocapillary effects. This result has been found when the liquid layer is considered in the Boussinesq approximation and with undeformable open surface. The critical (negative) Marangoni and (negative) Rayleigh numbers start at rather high absolute values for moderate Prandtl number fluids (e.g. the lowest possible absolute value of the Rayleigh number is 1.21×10^6 for $Pr = 6$ and $Bi = 0$), although achievable in standard experiments on low-viscosity liquids such as water. The convective heat transport in the air gap overlying the liquid is negligible when the air layer is relatively thin. Moreover, surface deformability is relevant only for thin, say sub-millimetre, liquid layers, while the Rayleigh–Marangoni instability described here is relevant for thicker layers in the centimetre range.

Marginal stability curves have been drawn, as Marangoni number versus wavenumber curves, either at fixed negative Rayleigh number, or at fixed *dynamic* Bond number, which is the ratio of the Rayleigh and Marangoni numbers. In the first case, the marginal curves have the form of a 'bubble' (figure 1*a*) enclosing the region of instability. The bubble size and shape crucially depend on the fixed Rayleigh number. As the Rayleigh number is increased (in absolute value), the bubble grows and rises to higher (absolute) values of the Marangoni number. In the second (more intuitive) case, the marginal curves have the usual, single-valued form (figure 2*a*). As the Bond number is increased, the minimum shifts from long to short waves. There exists an optimal Bond number (that in each particular case yields the optimal thickness of the liquid layer), for which the critical Marangoni number is lowest in absolute value. This corresponds to the optimal balance between buoyancy in the bulk and the Marangoni stress at the open surface, leading to instability. The instability threshold increases with the increase of Prandtl and Biot numbers.

An asymptotic analysis in the limit of high Marangoni and Rayleigh numbers (in absolute value) revealed that the oscillatory instability can be associated with two (high-frequency) wave modes: *internal* waves and *surface* waves. The first of them corresponds to the (Brunt–Väisälä) internal wave in a stably stratified liquid layer, while the second is the dilational or longitudinal surface wave appearing as a result of the Marangoni effect, hence corresponding to *genuinely dissipative* waves. It has been shown that the upper and lower branches of the bubble (figure 1*a*) tend to the marginal curves for the surface and internal waves, respectively. A *countable* number of bubbles (corresponding to different vertical wavenumbers $n = 1, 2 \ldots$) exists. It has

also been shown that the marginal curves at fixed dynamic Bond number (figure 2) always have vertical asymptotes, i.e. the interval of unstable wavenumbers remains finite for high Marangoni numbers (in absolute value). The branches of a given marginal curve adjacent to the left and right asymptotes correspond to *internal* and *surface* waves, respectively. The study of the resonance between these waves yields that, as we approach resonance, there is a smooth transition from the internal mode to the surface one and vice versa, and hence there is mode-mixing. Finally, a weakly nonlinear analysis showed that the bifurcation is supercritical and to standing (rather than traveling) waves.

The authors wish to express their appreciation to Professor H. Linde and Dr A. Wierschem for enlightening discussion and access to unpublished material. This work was supported by Fundación BBV (Programa Catedra in Cambridge University), by DGICYT (Spain) under Grants PB93-81 and PB96-599, by the Human Capital and Mobility Program of the European Union (under network ERBCHRXCT960010), and by the Belgian Program on Interuniversity Poles of Attraction (PAI IV-06) initiated by the Belgian State, Prime Minister's Office, Federal Office for Scientific, Technical and Cultural Affairs. P.C. also acknowledges financial support of the European Union through the Marie Curie fellowship no ERBFMBICT972099.

REFERENCES

Boer, P. C. T. de 1984 Thermally-driven motion of strongly heated fluids. *Intl J. Heat Mass Transfer* **27**, 2239–2251.

Boer, P. C. T. de 1986 Thermally-driven motion of highly viscous fluids. *Intl J. Heat Mass Transfer* **29**, 681–688.

Busse, F. H. 1978 Nonlinear properties of thermal convection. *Rep. Prog. Phys.* **41**, 1929–1967.

Chandrasekhar, S. 1961 *Hydrodynamic and Hydromagnetic Stability*. Clarendon.

Chu, X. L. & Velarde, M. G. 1988 Sustained transverse and longitudinal waves at the open surface of a liquid. *PhysicoChem. Hydrodyn.* **10**, 727–737.

Chu, X. L. & Velarde, M. G. 1989 Transverse and longitudinal waves induced and sustained by surfactant gradients at liquid-liquid interfaces. *J. Colloid Interface Sci.* **131**, 471–484.

Davis, S. H. & Segel, L. A. 1968 Effects of surface curvature and property variation on cellular convection. *Phys. Fluids* **11**, 470–476.

Earnshaw, J. C. & McLaughlin, A. C. 1991 Waves at liquid surfaces : coupled oscillators and mode mixing. *Proc. R. Soc. Lond.* A **433**, 663–678.

Earnshaw, J. C. & McLaughlin, A. C. 1993 Waves at liquid surfaces II. Surfactant action and coupled oscillators. *Proc. R. Soc. Lond.* A **440**, 519–536.

Garcia-Ybarra, P. L. & Velarde, M. G. 1987 Oscillatory Marangoni-Bénard interfacial instability and capillary-gravity waves in single- and two-component liquid layers with and without Soret thermal diffusion. *Phys. Fluids* **30**, 1649–1655.

Gershuni, G. Z. & Zhukhovitskii, E. M. 1976 *Convective Stability of Incompressible Fluids*. Keter-press, Jerusalem.

Hennenberg, M., Chu, X. L., Sanfeld, A. & Velarde, M. G. 1992 Transverse and longitudinal waves at the air-liquid interface in the presence of an adsorption barrier. *J. Colloid Interface Sci.* **150**, 7–21.

Knobloch, E. 1986 Oscillatory convection in binary mixtures. *Phys. Rev.* A **34**, 1538–1549.

Koschmieder, E. L. 1993 *Bénard Cells and Taylor Vortices*. Cambridge University Press.

Lamb, H. 1945 *Hydrodynamics*, 6th Edn. Dover.

Levchenko, E. B. & Chernyakov, A. L. 1981 Instability of surface waves in a nonuniformly heated liquid. *Sov. Phys. JETP* **54**, 102–105.

Levich, B. G. 1962 *Physicochemical Hydrodynamics*. Prentice-Hall.

Linde, H., Velarde, M. G., Wierschem, A., Waldhelm, W., Loeschke, R. & Rednikov, A. Ye.

1997 Interfacial wave motions due to Marangoni instability. I. Traveling periodic wavetrains in square and annular containers. *J. Colloid Interface Sci.* **188**, 16–26.

Lucassen, J. 1968*a* Longitudinal capillary waves. Part 1. Theory. *Trans. Faraday Soc.* **64**, 2221–2229.

Lucassen, J. 1968*b* Longitudinal capillary waves. Part 2. Experiments. *Trans. Faraday Soc.* **64**, 2230–2235.

Nield, D. A. 1964 Surface tension and buoyancy effects in cellular convection. *J. Fluid Mech.* **19**, 341–352.

Normand, C., Pomeau, Y. & Velarde, M. G. 1977 Convective instability: A physicist's approach. *Rev. Mod. Phys.* **49**, 581–624.

Pearson, J. R. 1958 On convective cells induced by surface tension. *J. Fluid Mech.* **4**, 489–500.

Perez-Cordon, R. & Velarde, M. G. 1975 On the (non linear) foundations of Boussinesq approximation applicable to a thin layer of fluid. *J. Phys.* (*Paris*) **36**, 591–601.

Rayleigh, Lord 1916 On convective currents in a horizontal layer of fluid, when the higher temperature is on the under side. *Phil. Mag.* **32**, 529–546.

Rednikov, A. Ye., Colinet, P., Velarde, M. G. & Legros, J. C. 1998 Two-layer Bénard-Marangoni instability and the limit of transverse and longitudinal waves. *Phys. Rev.* E **57**, 2872–2884.

Reichenbach, J. & Linde, H. 1981 Linear perturbation analysis of surface-tension-driven convection at a plane interface (Marangoni instability). *J. Colloid Interface Sci.* **84**, 433–443.

Renardy, Y. Y. 1993 Pattern selection for the oscillatory onset in thermosolutal convection. *Phys. Fluids* A **5**, 1376–1389.

Sternling, C. V. & Scriven, L. E. 1959 Hydrodynamic instability and the Marangoni effect. *AIChE J.* **5**, 514–523.

Takashima, M. 1981 Surface tension driven instability in a horizontal liquid layer with a deformable free surface. II Overstability. *J. Phys. Soc. Japan* **50**, 2751–2756.

Velarde, M. G., Linde, H., Nepomnyashchy, A. A. & Waldhelm, W. 1995 Further evidence of solitonic behavior in Marangoni- Bénard convection: periodic wave trains. In *Fluid Physics* (ed. M. G. Velarde & C. I. Christov), pp. 433–441. World Scientific.

Velarde, M. G. & Normand, Ch. 1980 Convection. *Sci. Am.* **243**, 1, 92–108.

Velarde, M. G. & Perez-Cordon, R. 1976 On the (non linear) foundations of Boussinesq approximation applicable to a thin layer of fluid (II) Viscous dissipation and large cell gap effects. *J. Phys.* (*Paris*) **37**, 177–182.

Vidal, A. & Acrivos, A. 1966 Nature of the neutral state in surface tension driven convection. *Phys. Fluids* **9**, 615–616.

Weidman, P. D., Linde, H. & Velarde, M. G. 1992 Evidence for solitary wave behavior in Marangoni-Bénard convection. *Phys. Fluids* A **4**, 921–926.

Wierschem, A., Velarde, M. G., Linde, H. & Waldhelm, W. 1999 Interfacial wave motions due to Marangoni instability. II. Three-dimensional characteristics of surface-waves in annular containers. *J. Colloid Interface Sci.* **212**, 365–383.